Real-time monitoring of metabolic function in liver-on-chip microdevices tracks the dynamics of mitochondrial dysfunction

Danny Bavli[a,b,1], **Sebastian Prill**[c,1], **Elishai Ezra**[a], **Gahl Levy**[a], **Merav Cohen**[a,b], **Mathieu Vinken**[d], **Jan Vanfleteren**[e,f], **Magnus Jaeger**[c,g], **and Yaakov Nahmias**[a,b,2]

[a]Alexander Grass Center for Bioengineering, The Hebrew University of Jerusalem, Jerusalem 91904, Israel; [b]Department of Cell and Developmental Biology, Silberman Institute of Life Sciences, The Hebrew University of Jerusalem, Jerusalem 91904, Israel; [c]Branch Bioanalytics and Bioprocesses, Fraunhofer Institute for Cell Therapy and Immunology, Potsdam 14476, Germany; [d]Department of in Vitro Toxicology and Dermato-Cosmetology, Vrije Universiteit Brussel, Brussels 1090, Belgium; [e]Centre for Microsystems Technology, Ghent University, Ghent B-9052, Belgium; [f]Imec, Ghent B-9052, Belgium; and [g]Federal Institute for Risk Assessment, Berlin 10589, Germany

Edited by David A. Weitz, Harvard University, Cambridge, MA, and approved March 7, 2016 (received for review November 16, 2015)

Microfluidic organ-on-a-chip technology aims to replace animal toxicity testing, but thus far has demonstrated few advantages over traditional methods. Mitochondrial dysfunction plays a critical role in the development of chemical and pharmaceutical toxicity, as well as pluripotency and disease processes. However, current methods to evaluate mitochondrial activity still rely on end-point assays, resulting in limited kinetic and prognostic information. Here, we present a liver-on-chip device capable of maintaining human tissue for over a month in vitro under physiological conditions. Mitochondrial respiration was monitored in real time using two-frequency phase modulation of tissue-embedded phosphorescent microprobes. A computer-controlled microfluidic switchboard allowed contiguous electrochemical measurements of glucose and lactate, providing real-time analysis of minute shifts from oxidative phosphorylation to anaerobic glycolysis, an early indication of mitochondrial stress. We quantify the dynamics of cellular adaptation to mitochondrial damage and the resulting redistribution of ATP production during rotenone-induced mitochondrial dysfunction and troglitazone (Rezulin)-induced mitochondrial stress. We show troglitazone shifts metabolic fluxes at concentrations previously regarded as safe, suggesting a mechanism for its observed idiosyncratic effect. Our microfluidic platform reveals the dynamics and strategies of cellular adaptation to mitochondrial damage, a unique advantage of organ-on-chip technology.

microfluidics | liver tissue engineering | toxicology | organ-on-a-chip

Microfluidic organ-on-a-chip devices offer an alternative to animal experiments due to their ability to mimic physiological parameters, such as shear or mechanical forces, acting on human cells in vitro. Using a lung-on-chip device, Huh et al. (1) demonstrated that mechanical forces are critical for the development of nanoparticle toxicity in lung tissue, while our group and others demonstrated the long-term maintenance of hepatocyte function in a microfluidic bioreactor (2–5). Regretfully, most organ-on-chip devices still rely on endpoint assays to assess drug toxicity, providing limited dynamic information that can be used to assess the compound mechanism of action (6, 7).

Mitochondrial function plays a critical role in the development of disease and chemical toxicity (7, 8), as well as the regulation of stem cell pluripotency (9). Mitochondrial dysfunction can occur through direct damage to the respiratory chain, or through secondary mechanisms such as ER stress or lipid accumulation (10). Because cells can adapt to loss of mitochondrial respiration by using anaerobic pathways such as glycolysis and glutaminolysis (Fig. 1*A*), mitochondrial damage can often go undetected with disastrous clinical and financial consequences (8), which is a particular concern in cultured cells that show an increased reliance on glycolysis and glutaminolysis due to the Warburg effect. Thus, real-time monitoring of these metabolic fluxes could provide critical insight into the development of mitochondrial dysfunction, as well as loss and gain of mitochondrial function in development.

Recently, we demonstrated the real-time measurement of oxygen uptake in liver-on-chip devices using two-frequency phase modulation of tissue-embedded phosphorescent microprobes (11). Oxygen decreases phosphorescence decay time resulting in a phase change that is independent of signal intensity. In contrast to other methods, phase modulation is unaffected by focus distance or changing microprobe concentration due to cell death or migration, thus providing unparalleled ability to monitor oxygen uptake in real-time. Our design offers clear advantage over Clark-type electrodes that consume oxygen and require precise positioning and frequent recalibration (12). However, oxygen measurements provide only circumstantial evidence to loss of mitochondrial function.

In this work, we report the development of a liver-on-chip device capable of maintaining 3D aggregates of HepG2/C3A cells for over 28 d in vitro under physiological shear forces and stable oxygen gradient mimicking the native liver microenvironment. Oxygen uptake rate is monitored in real time using two-frequency phase modulation, while a computer controlled microfluidic switchboard automates washing, calibration, and amperometric measurements of glucose uptake and lactate production over the same time period (Fig. 1*B*). Our system permits the detection of minute shifts from oxidative phosphorylation to glycolysis or glutaminolysis, indicating mitochondrial damage in drug concentrations previously believed to be safe. Our precise measurements permit a unique analysis of the redistribution of ATP production in cells undergoing mitochondrial stress and dysfunction, unraveling the unique dynamics of the metabolic adaptation to mitochondrial damage.

Significance

Microfluidic organ-on-a-chip technology is poised to replace animal toxicity testing, but thus far has demonstrated few advantages over traditional methods. Here we demonstrate a sensor-integrated platform permitting real-time tracking of the dynamics of metabolic adaptation to mitochondrial dysfunction. Our approach permits detection of chemical toxicity before any effects on cell or tissue viability can be observed.

Author contributions: Y.N. designed research; D.B., S.P., E.E., G.L., M.C., and Y.N. performed research; J.V. and M.J. contributed new reagents/analytic tools; D.B., S.P., E.E., G.L., M.V., and Y.N. analyzed data; and D.B., S.P., G.L., and Y.N. wrote the paper.

The authors declare no conflict of interest.

This article is a PNAS Direct Submission.

[1] D.B. and S.P. contributed equally to this work.

[2] To whom correspondence should be addressed. Email: ynahmias@cs.huji.ac.il.

This article contains supporting information online at www.pnas.org/lookup/suppl/doi:10.1073/pnas.1522556113/-/DCSupplemental.

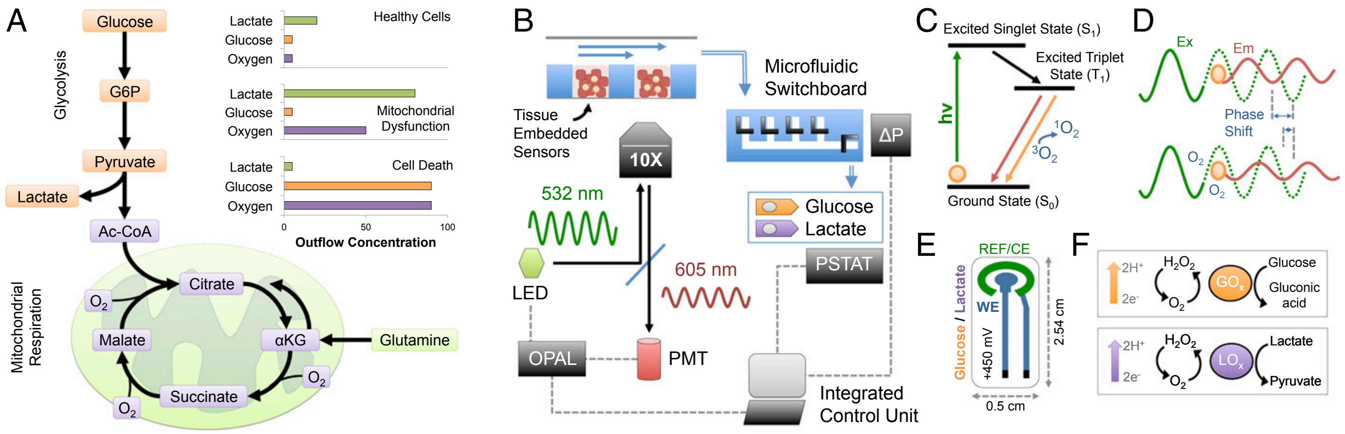

Fig. 1. (*A*) Schematic of glucose and glutamine utilization by central carbon metabolism. Theoretically, mitochondrial dysfunction will lead to a decrease in oxygen uptake and increase in lactate production due to cellular shift from oxidative phosphorylation (purple) to glycolysis (orange). (*B*) Scheme of the measurement setup. Bioreactor was loaded with tissue-embedded oxygen sensors and mounted on an Olympus IX83. OPAL unit controlled LED signal modulation, exciting the oxygen sensors, and analyzed the signal through the photomultiplier readout. Bioreactor outflow was connected to a microfluidic switchboard containing a series of pressure-controlled micromechanical valves. The switchboard introduced samples into a sensor unit containing electrochemical sensors for glucose and lactate. Sensors were controlled by a potentiostat (PSTAT). Optical, pressure, and electronic sensors were connected to a single microprocessor that synchronized the signal. (*C*) Jablonski diagram describing the generation of phosphorescence with Ru-CPOx beads under the influence of oxygen. The quenching of the phosphorescence by triplet oxygen leads to a decrease in signal intensity and phosphorescence decay time (T_1). (*D*) The effect described in *C* induces a phase shift between the intensity-modulated excitation and emission light. Thus, the degree of phase shift can be used for determining the oxygen concentration. Two-superimposed frequencies were used to screen out background interference. (*E*) Design of amperometric sensor in two-electrode configuration. Anodic oxidation of H_2O_2 on the platinum working-electrode (WE) held at 450 mV against the reference electrode (REF/CE) produces a detected current. (*F*) H_2O_2 is created in equivalent amounts of the analyte as an intermediate product by the activity of glucose oxidase (GO_x) or lactate oxidase (LO_x).

Results

System Design. Mitochondrial dysfunction is a major cause of drug-induced injury due to the limited ability of cells to generate ATP by alternatives means. Increasing glycolysis, fermentation of glucose to lactate, is the preferred route of energy production in the absence of oxygen (Fig. 1*A*). Glutamine degradation to lactate and citrate, termed glutaminolysis, can also support tumor cell growth under hypoxic conditions. Our hypothesis was that mitochondrial damage would lead to rapid compensation, as cells shift from mitochondrial respiration to glycolysis to survive. To monitor the dynamic transition between these metabolic pathways, we designed a microfluidic system that maintains growth-arrested HepG2/C3A spheroids under physiological conditions while dynamically measuring oxygen, glucose, and lactate concentrations (Fig. 1*B*).

Oxygen is measured using tissue-embedded microparticles loaded with a ruthenium-based dye, whose phosphorescence is quenched in the presence of oxygen leading to decreasing decay time (Fig. 1*C*). In contrast to intensity measurement, decay time is insensitive to probe concentration or excitation intensity. We use sinusoidal intensity-modulated light, resulting in an oxygen-dependent phase shift in the 605-nm emission (Fig. 1*D*). Using our system, the signal is stable down to three particles, and 1.5 mm away from the microscope focus (11). In contrast to optical measurements, electrochemical sensors require frequent recalibration and demonstrate significant decay over time. Therefore, we chose to integrate off-the-shelf medical-grade sensors in our microfluidic design, and address them using a computer-controlled microfluidic switchboard that sequentially samples the bioreactor outflow, washes and recalibrates the sensors. Our amperometric glucose and lactate sensors use platinum electrodes to measure current under a polarization of 450 mV (Fig. 1*E*). Current is produced by the oxidation of glucose or lactate to H_2O_2 by membrane-embedded glucose or lactate oxidase (Fig. 1*F*). A single central processing unit (CPU) controls the entire system, simplifying synchronization (13).

Design and Characterization of Hepatic Microwell Bioreactor. The liver is highly vascularized, delivering oxygen at high rates while protecting hepatocytes from the negative effects of shear (14, 15). The gradients that develop along the sinusoid induce a demarcation of function, termed metabolic zonation. To mimic this environment we designed a polymethyl methacrylate (PMMA) bioreactor with a detachable multiwell unit that permits cell seeding in an open configuration (Fig. 2 *A* and *B*). HepG2/C3A cells mixed with oxygen probes were seeded in the microwells protecting the cells from the negative effect of shear forces while providing a constant concentration of nutrients and removal of metabolic waste products. Cells aggregate to spheroids after overnight incubation (Fig. 2*C*), polarizing and reaching growth arrest in 4–7 d in the presence of 1% (vol/vol) DMSO (16, 17).

Computational fluid dynamic modeling (Fig. 2 *D* and *E*) showed physiological shear forces under 0.03 Pa inside the microwells for perfusion rates of 2 μL/min. The flow rate resulted in similar oxygen concentration delivered to each well in the array (Fig. 2 *D* and *E*). Oxygen consumption caused a gradient to develop along the perfused spheroid, mimicking the in vivo microenvironment (Fig. 2*E*) (18, 19). Glucose concentration showed a similar gradient, reaching 0.1 mM concentration at the bottom of the microwells. These results suggest our reactor mimics aspects of the physiological microenvironment. Oxygen uptake was measured in real time over 28 d under continuous perfusion (Fig. 2*F*). Measurement showed an increase in oxygen uptake, stabilizing on day 4, suggesting the cells reached steady state. Gene expression on day 30 of culture showed marked elevation of liver-specific gene expression compared with static culture (Fig. 2*G*). Primarily, expression of the Pregnane X receptor (*PXR*) and the constitutive androstane receptor (*CAR*) increase by 10- and 18-fold, respectively ($P < 0.024$, $n = 3$), whereas their target genes *MDR1*, *CYP2C9*, and *CYP3A4* showed 20- to 300-fold increase in mRNA abundance ($P < 0.022$, $n = 3$).

Real-Time Oxygen Measurement Shows Rapid Loss of Mitochondrial Respiration. Rotenone is a widely used broad-spectrum organic insecticide and pesticide, known to directly damage mitochondrial

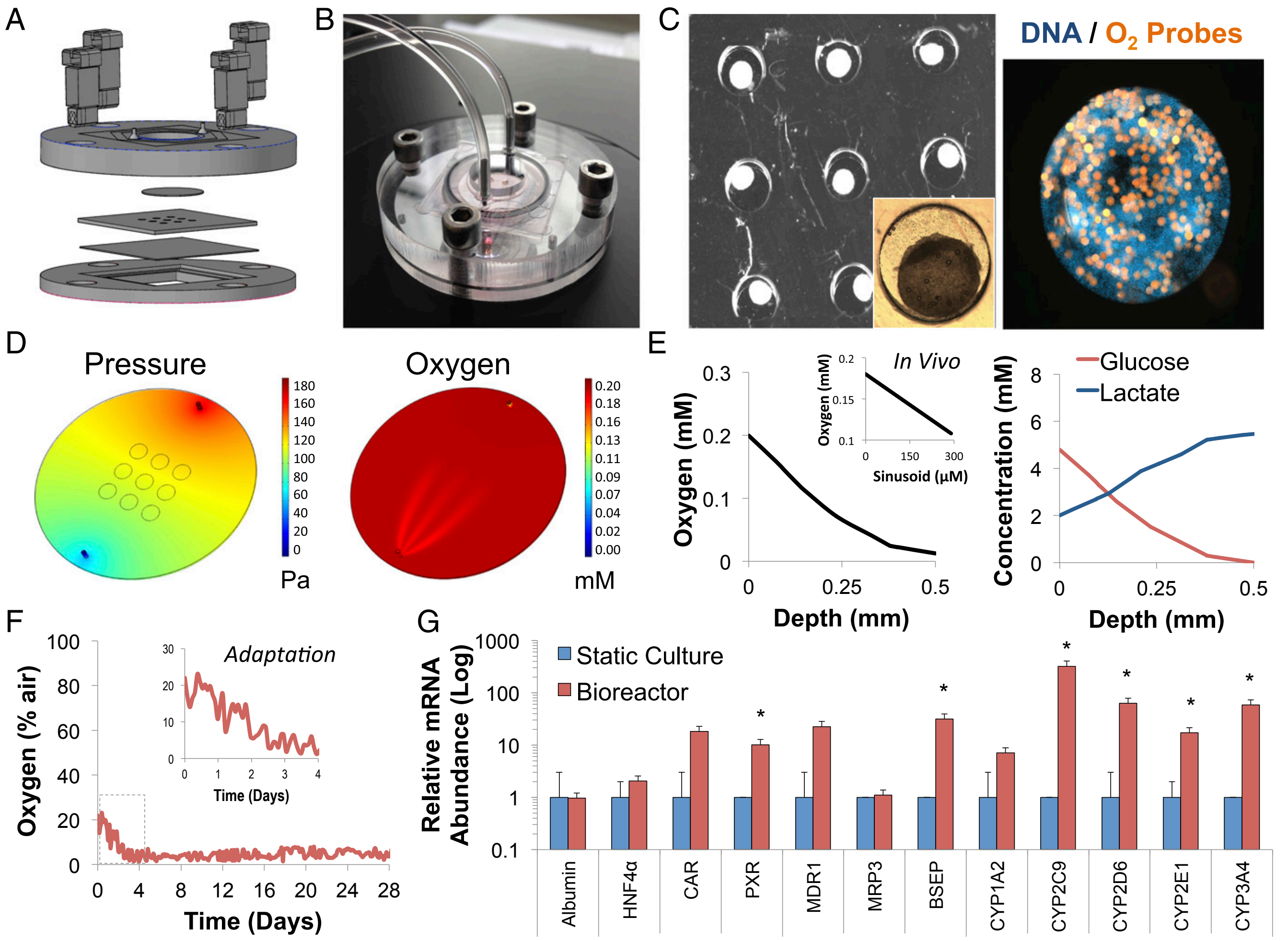

Fig. 2. (*A*) Explosive view of bioreactor components. From bottom to top: PMMA housing, cover glass, laser-cut PDMS microwells, top glass window, and PMMA cover. (*B*) Photo of assembled bioreactor on microscope stage. (*C*) Composite tile scan image of HepG2/C3A organoid after overnight incubation with embedded oxygen-sensing microprobes (orange). (*D*) Numerical simulation of the pressure drop and variations in oxygen concentration throughout the bioreactor. (*E*) Cross-section of oxygen gradient developing due to consumption within the well (from top to bottom), mimicking the in vivo microenvironment. (*Right*) Gradients of glucose and lactate concentrations within the well. (*F*) Representative long-term oxygen measurement over 1 mo in bioreactor perfused with cell culture medium at 2 μL/min. One hundred percent air represents atmospheric dissolved oxygen concentration (no consumption). Cultures reach steady state within 4 d after seeding. (*G*) Log-scale quantitative gene expression analysis of HepG2/C3A cells in static culture compared with those perfused with 1% DMSO for 30 d (growth arrest). PXR, CYP3A4 and CYP2C9 expression shows a 10-, 58-, and 300-fold increase in the bioreactor, respectively ($P < 0.024$, $n = 3$). Values are within 10–30% of primary human hepatocytes. $^*P < 0.05$ by Student's *t* test.

complex I, inducing oxidative stress and apoptosis at low concentrations (20). Rotenone was perfused at concentrations of 1, 50, and 200 μM for 24 h, and oxygen uptake of the cells was monitored in real time to assess cell viability and metabolic function (Fig. 3*A*). Oxygen uptake dropped rapidly when cells were exposed to 1, 50, and 200 μM rotenone, reaching 35%, 27%, and 15% of normal respiration following 12-h exposure, respectively. The majority of the effect occurred within the first 60 min, as expected from a direct complex I inhibitor. Plotting the dose-dependent response of rotenone at 12 h, we calculate a TC$_{50}$ of 12.5 μM in our system (Fig. 3*B*), compared with 2 μM in primary hepatocytes. To evaluate the toxicological end point of rotenone, we quantified the number of intact and apoptotic nuclei using the TUNEL assay (Fig. 3*C*). Cells exposed to rotenone showed a 14 ± twofold increase in apoptosis ($P < 0.001$, $n = 5$), as well as unlabeled cell death, suggesting necrosis.

Troglitazone is an antidiabetic and anti-inflammatory drug that was removed from market due to severe drug-induced liver injury (21). Though troglitazone mechanism of action is still unclear, its metabolites were shown to block bile acid transporters BSEP and MRP2, leading to cholestasis, whereas the parent compound was shown to decrease mitochondrial membrane potential (22). Troglitazone was perfused at concentrations ranging from 50 to 2,000 μM for 24 h, and oxygen uptake of the cells was monitored in real time to assess cell viability and metabolic function (Fig. 3*D*). Oxygen concentration at 50 μM troglitazone was not significantly different from control. However, oxygen uptake dropped when cells were exposed to 350, 500, and 2,000 μM troglitazone, reaching 32%, 15%, and 8% of normal respiration following 24-h exposure, respectively. Interestingly, most of the effect occurred within the first 5 h, suggesting direct mitochondrial damage rather than accumulation of secondary metabolites (11). Plotting the dose-dependent response of troglitazone at 24 h, we calculate a TC$_{50}$ of 285 μM in our system (Fig. 3*E*), compared with 100 μM in primary hepatocytes. To evaluate the toxicological end point of troglitazone, we evaluated 5(6)-carboxy-2′,7′-dichlorofluorescein (CDF) retention in treated and untreated cells (Fig. 3*F*). Cells exposed to troglitazone showed a 4.5 ± 0.6-fold increase in CDF staining due to inhibition of MRP2 ($P < 0.001$, $n = 5$).

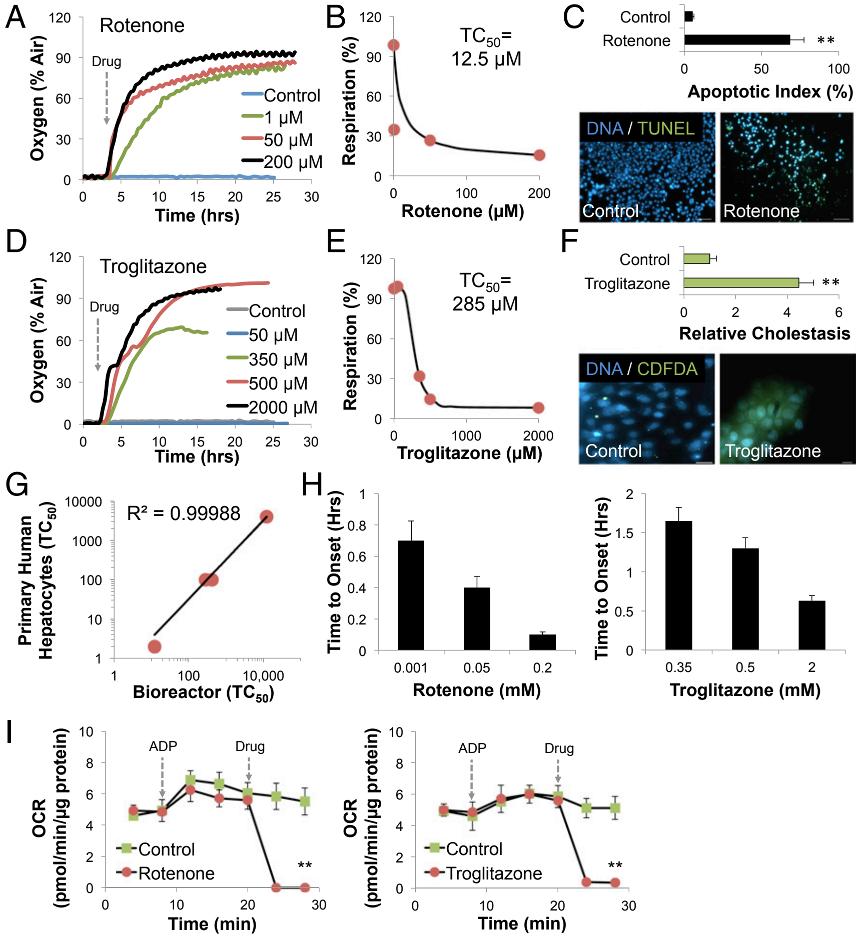

Fig. 3. (*A*) Representative oxygen uptake over time response of HepG2/C3A cells exposed to increasing concentrations of rotenone. (*B*) Dose dependence of rotenone after 12 h. TC$_{50}$ was calculated to be 12.5 μM. (*C*) TUNEL staining shows 14-fold increase in apoptosis following 24 h exposure to 200 μM rotenone ($P < 0.001$, $n = 5$), as well as unlabeled cell death, suggesting necrosis. (*D*) Representative oxygen uptake over time response of HepG2/C3A cells exposed to increasing concentrations of troglitazone. (*E*) Dose dependence of troglitazone after 24 h. TC$_{50}$ was calculated to be 285 μM. (*F*) CDFDA staining shows 4.5-fold increase in intracellular accumulation of bile acids (cholestasis) following 24-h exposure to 200 μM troglitazone ($P < 0.001$, $n = 5$). (*G*) IVIVC curve comparing TC$_{50}$ values of primary human hepatocytes to our bioreactor showing an excellent $R^2 = 0.99$ correlation for acetaminophen, amiodarone, troglitazone, and rotenone. (*H*) Time to onset of mitochondrial damage was dose dependent for both rotenone (*Left*) and troglitazone (*Right*), occurring in minutes rather than hours following exposure to the drugs. (*I*) OCR measured on isolated mitochondria for 30 min, followed by ADP injection (arrow) and subsequent injection of 50 μM rotenone (*Left*) or troglitazone (*Right*). Loss of OCR was immediate ($P < 0.001$, $n = 3$) and did not require cytosolic enzyme activation of the drugs. **$P < 0.01$ by Student's *t* test.

Overall, comparison of our bioreactor results to primary human hepatocytes (IVIVC) across four drugs, including acetaminophen, amiodarone, troglitazone, and rotenone showed an R^2 of 0.99 (Fig. 3*G*). Interestingly, both rotenone and troglitazone showed a dose-dependent time to onset of damage (Fig. 3*H*). Rotenone acted within 6 min of administration at 0.2 mM, whereas troglitazone showed respiratory damage within 40–100 min. The dynamics of these responses suggest that both compounds directly damage the mitochondria, rather than produce a slow accumulation of toxic intermediates. To evaluate this, we measured oxygen consumption rates (OCR) of ADP-stimulated isolated mitochondria (Fig. 3*I*). We show that troglitazone, like rotenone, can directly inhibit mitochondrial respiration in minutes ($P < 0.001$, $n = 3$) in the absence of enzymatic activation.

Automated Microfluidic Measurement of Glucose and Lactate. Electrochemical sensors have a limited lifespan and require frequent recalibration. Therefore, we fabricated an off-chip sensor unit (Fig. 4*A*) containing off-the-shelf medical-grade sensors. Accurate measurement required a sharp chemical gradient, which we achieved by purging the system with air before each measurement, producing a linear response of glucose and lactate sensors up to 20 mM (Fig. 4*B*). To carry out the experimental steps automatically, we fabricated a microfluidic switchboard containing 12 self-addressable micromechanical valves (Fig. 4*C*) connected to a 32-bit ARM7-based control unit that synchronizes flow, measurement, and stimulation (13). Micromechanical valves were fabricated using two-layer soft lithography showing an actuation pressure of 4 psi and stability for over 15,000 cycles, 150–300 d at our sampling rate (Fig. 4*D*). Bioreactors were continuously perfused with their outflow split into a high-resistance waste and the valve-controlled switchboard (Fig. 4*E*). Samples were obtained every hour by opening the valve for 20 min and permitting a 40-μL sample to be introduced into the sensor unit. Sampling was preceded and followed by a 4-s purging with air (Fig. 4 *E* and *F*), creating a sharp concentration step-change. A 200-s washing step was intertwined between sampling and calibration steps. The entire sequence was 23.3 min long, permitting a measurement of three bioreactors per hour.

At steady state, glucose and lactate concentration at the bioreactor outflow were 2.9 mM and 5 mM, respectively (Fig. 4 *G* and *H*). Cell number was quantified by DNA content to be 10^5 cells/well, resulting in glucose uptake rate of 2.4×10^{-9} mol·min^{-1} per 10^6 cells and lactate production rate of 3×10^{-9} mol·min^{-1} per 10^6 cells under steady-state conditions (Fig. S1). Each mole of glucose can produce 2 mol of lactate in anaerobic glycolysis, or use 6 mol of oxygen in oxidative phosphorylation (Fig. 1*A*). Our results show a lactate over glucose ratio of 1.3 for our cells, suggesting that 62% of glucose is used in glycolysis. Together with our oxygen measurements (Fig. 2), we suggest that 13% of glucose consumed is directed toward oxidative phosphorylation with 26% directed toward other metabolic pathways such as lipogenesis. To exclude fatty acid oxidation, we measured their uptake rate in the bioreactor outflow. Fatty acid uptake was 4.8×10^{-11} mol·min^{-1} per 10^6 cells, about 50-fold lower than glucose uptake. Glutamine uptake was 1.6×10^{-10} mol·min^{-1} per 10^6 cells (Fig. S2), 10-fold lower than glucose uptake, suggesting glutaminolysis had a minor contribution to the mitochondrial Krebs cycle, which was predominantly using glucose as a source of energy in steady state (Fig. 1*A*). We note that proliferating HepG2 cells exhibit quite a different metabolic signature under static conditions, showing lactate over glucose ratio ranging from 1.8 to 2.

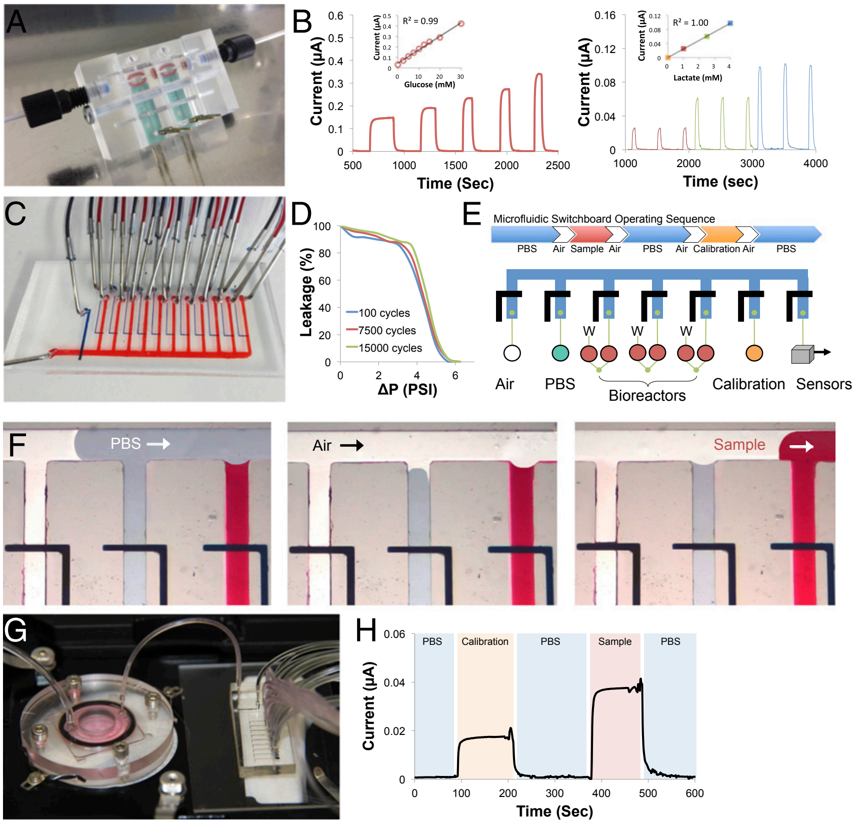

Fig. 4. (*A*) Photo of PMMA unit housing both glucose and lactate sensors with total internal volume of 26 μL. (*B*) Amperometric calibration curves of glucose and lactate sensors in the PMMA housing. Measurements were carried out under static condition for 100–200 s. Air purging before sample introduction ensured sharp change in chemical gradient. (*C*) Photo of two-layer microfluidic switchboard containing flow channels (red) and independently addressed control channels (blue). (*D*) Characterization of micromechanical valve switching pressure as a function of number of cycles (age). Valves withstand over 15,000 cycles without loss of sensitivity, up to 300 d of continuous operation. (*E*) Schematic of microfluidic switchboard connectivity and operating sequence. Switchboard contained inputs to air, washing buffer (PBS), and calibration solution. Bioreactors outflow was split to high-resistance waste (W) and normally closed channel to switchboard. Air purging was carried out for 4 s before and after measurement or calibration step. A total of 200 s of washing intersected between measurements. (*F*) Images of perfusion sequence starting with a washing step (blue), air purging, and sample introduction (red). (*G*) Photo of simplified setup where a single bioreactor is connected to the switchboard. (*H*) Automatic amperometric calibration and measurement of glucose concentration in bioreactor outflow.

Dynamics of Drug-Induced Mitochondrial Dysfunction. Drug-induced mitochondrial dysfunction is often overlooked due to the ability of cells to circumvent damaged metabolic pathways at low drug concentrations, and secondary effects, such as apoptosis becoming dominant at increasing concentrations. To characterize the dynamics of mitochondrial dysfunction, we exposed the cells to low concentrations of rotenone or troglitazone. Rotenone is a direct inhibitor of mitochondrial respiration, reducing oxygen uptake by 80% (Fig. 3 *A* and *B*) but inducing less than 15% cell death at 50 μM concentration (Fig. 5*A*). Real-time glucose and lactate measurements showed a sharp 59% drop in glucose uptake mirrored by a 35% drop in lactate production within the first 2 h (Fig. 5*B*). Lactate over glucose ratio increased from 1.5 to 2.6, demonstrating a strong shift toward glycolysis, coupled with a rapid loss of oxygen uptake (Fig. 5*C*). Cellular death became apparent after 6 h of exposure to rotenone, with an additional 65% drop in glucose uptake, but surprisingly no change in lactate production. Lactate over glucose ratio increased from 2.6 to 6.1, suggesting that glucose was no longer the main source for lactate production as the cells shifted toward glutaminolysis while drifting toward apoptosis (Fig. 3*C*). Indeed, offline measurement showed 30 ± 4-fold increases in glutamine consumption (Fig. S2) following rotenone exposure ($P < 0.007$, $n = 3$).

At 50 μM concentration, troglitazone reduced oxygen uptake rate by 10% (Fig. 3 *D* and *E*), while cell viability was not significantly different from untreated control (Fig. 5*D*). Surprisingly, though glucose uptake remained relatively unchanged, lactate production increased by 51% within 4–5 h (Fig. 5*E*). Lactate over glucose ratio increase from 1.3 to 1.8, demonstrating a clear shift toward glycolysis at concentrations below the threshold of troglitazone toxicity (Fig. 5*F*). Offline measurement showed a mild 5 ± 2-fold increase in glutamine consumption (Fig. S2) following troglitazone exposure ($P < 0.04$, $n = 3$).

Metabolic Adaptation and Redistribution of ATP Production. Our results demonstrate differential metabolic response to mild or severe damage to the respiratory chain, exemplified by troglitazone and rotenone exposure, respectively (Figs. 5–7). Because the flux balance stoichiometry is known (Methods), our data allows us to estimate intracellular fluxes (Table 1) and predict ATP production under each condition (Fig. 5*G*).

Troglitazone-induced mitochondrial stress caused a 23% decrease in oxidative phosphorylation and 51% increase in glycolysis after 6 h of exposure (Table 1). Glucose was no longer directed toward other metabolic pathways (Fig. 7) and was entirely used for

Table 1. Calculated metabolic fluxes in nmol·min^{-1} per 10^{6} cells for untreated cells (normal), troglitazone-treated cells (mitochondrial stress), and rotenone-treated cells (mitochondrial dysfunction)

Condition	Glycolysis	Respiration	Glutaminolysis	Lipogenesis
Normal	1.49	0.31	0	0.62
Mitochondrial stress	2.25	0.25	0.02	0
Mitochondrial dysfunction	0.97	0.03	0.56	0

Total glucose uptake rate was 2.4 nmol·min^{-1} per 10^{6} for untreated cells, 2.5 nmol·min^{-1} per 10^{6} for troglitazone-treated cells, and 1.0 nmol·min^{-1} per 10^{6} for rotenone-treated cells.

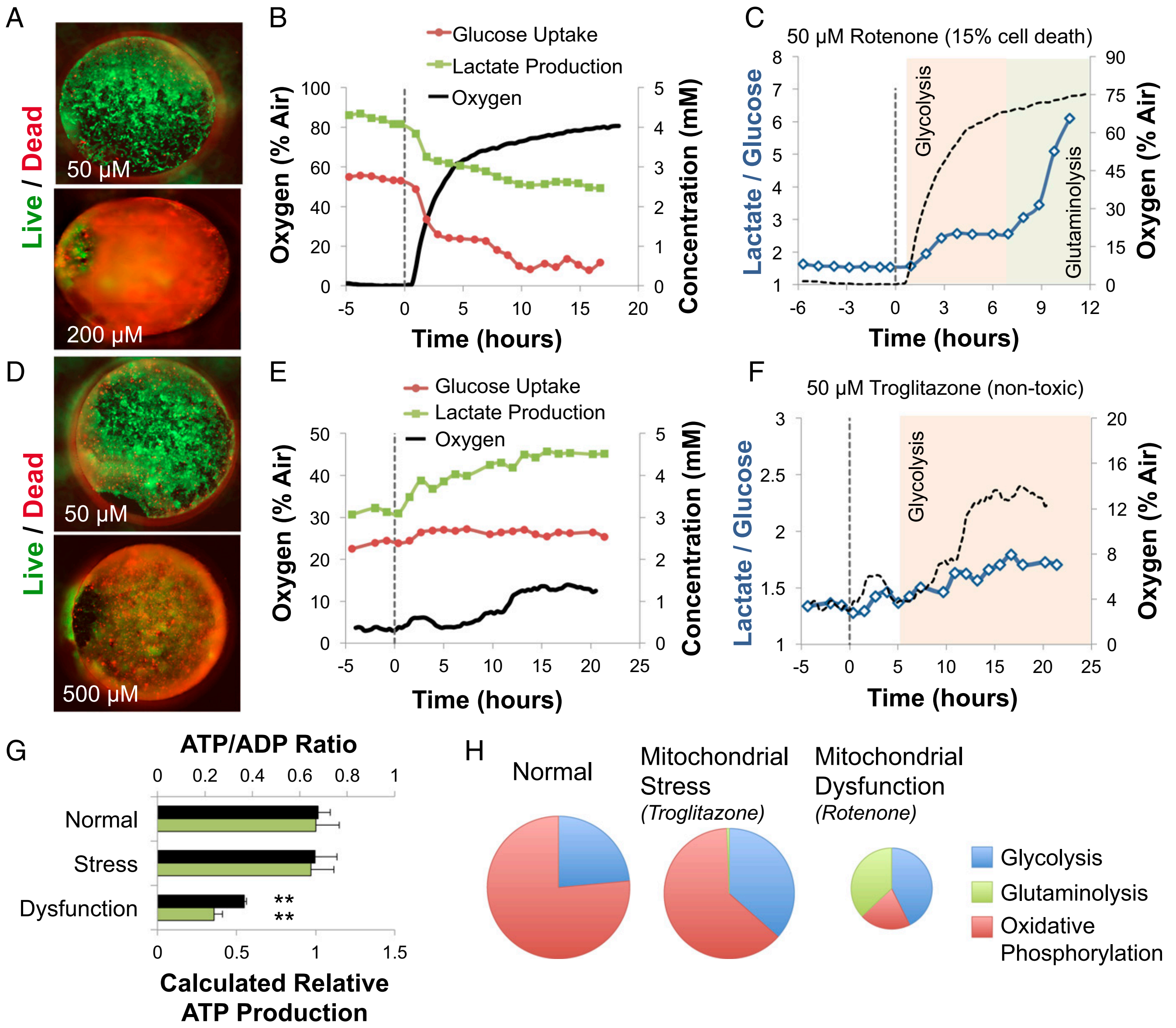

Fig. 5. (*A*) Composite tile scan image of live/dead staining of HepG2/C3A organoids in bioreactors treated for 24 h with 50 or 200 μM rotenone. Approximately 15% of the cells died following exposure to 50 μM rotenone. (*B*) Representative curves of oxygen uptake, glucose uptake, and lactate production of HepG2/C3A cells following exposure to 50 μM rotenone (dotted line). Glucose uptake is shown as inlet–outlet concentration (red circles), whereas lactate production is shown as outlet–inlet concentration (green squares). (*C*) Changes in lactate over glucose ratio following exposure to rotenone (dotted line). Ratio shifts from 1.5 to 2.6 within 3 h after exposure, indicating a shift from oxidative phosphorylation to glycolysis. Ratio spirals to 6.1 after 6 h exposure followed by increase in cell death. (*D*) Composite tile scan image of live/dead staining of HepG2/C3A organoids in bioreactors treated for 24 h with 50 or 200 μM troglitazone. Less than 5% of the cells died following exposure to 50 μM troglitazone, not significantly different from control. (*E*) Representative curves of oxygen uptake, glucose uptake, and lactate production of HepG2/C3A cells following exposure to 50 μM troglitazone (dotted line). (*F*) Changes in lactate over glucose ratio following exposure to troglitazone (dotted line). Ratio gradually shifts from 1.3 to 1.8 within 6 h after exposure, indicating a shift from oxidative phosphorylation to glycolysis. (*G*) Relative ATP production rate calculated from flux balance analysis (Table 1; *Methods*), juxtaposed with experimentally measured ATP/ADP ratio in troglitazone-, rotenone-, and vehicle-treated cells. Rotenone-treated cells show 47% decrease in ATP/ADP ratio ($P < 0.001$, $n = 3$), whereas troglitazone-treated cells show no significant difference despite the metabolic shift. (*H*) Diverging metabolic sources of ATP production in untreated cells (normal), troglitazone-treated cells (mitochondrial stress), and rotenone-treated cells (mitochondrial dysfunction) presented as pie charts of relative diameter.

ATP production (Fig. 5 *G* and *H*). These metabolic shifts, together with mild up-regulation of glutaminolysis (Fig. S2), allowed troglitazone-treated cells to maintain 97% of ATP production of untreated cells (Fig. 5*G*). Direct measurement of ATP/ADP ratio confirms our predictions (Fig. 5*G*).

In contrast, rotenone-induced mitochondrial dysfunction caused a 90% decrease in oxidative phosphorylation flux and 34% increase in glycolysis after 3 h of exposure (Table 1). Moreover, lactate production outpaced glucose uptake, suggesting glutaminolysis started playing a role in energy production, confirmed by offline measurements of glutamine uptake (Fig. 7; Fig. S2). Despite these metabolic shifts, ATP production of rotenone-treated cells was less than 36% of untreated cells (Fig. 5 *G* and *H*). Direct measurement of ATP/ADP ratio confirms our predictions ($P < 0.001$, $n = 3$).

Pathway Validation Under Static Conditions. To confirm our findings, we exposed static cultures of HepG2/C3A cells to 50 μM of rotenone and troglitazone and stained for mitochondrial membrane

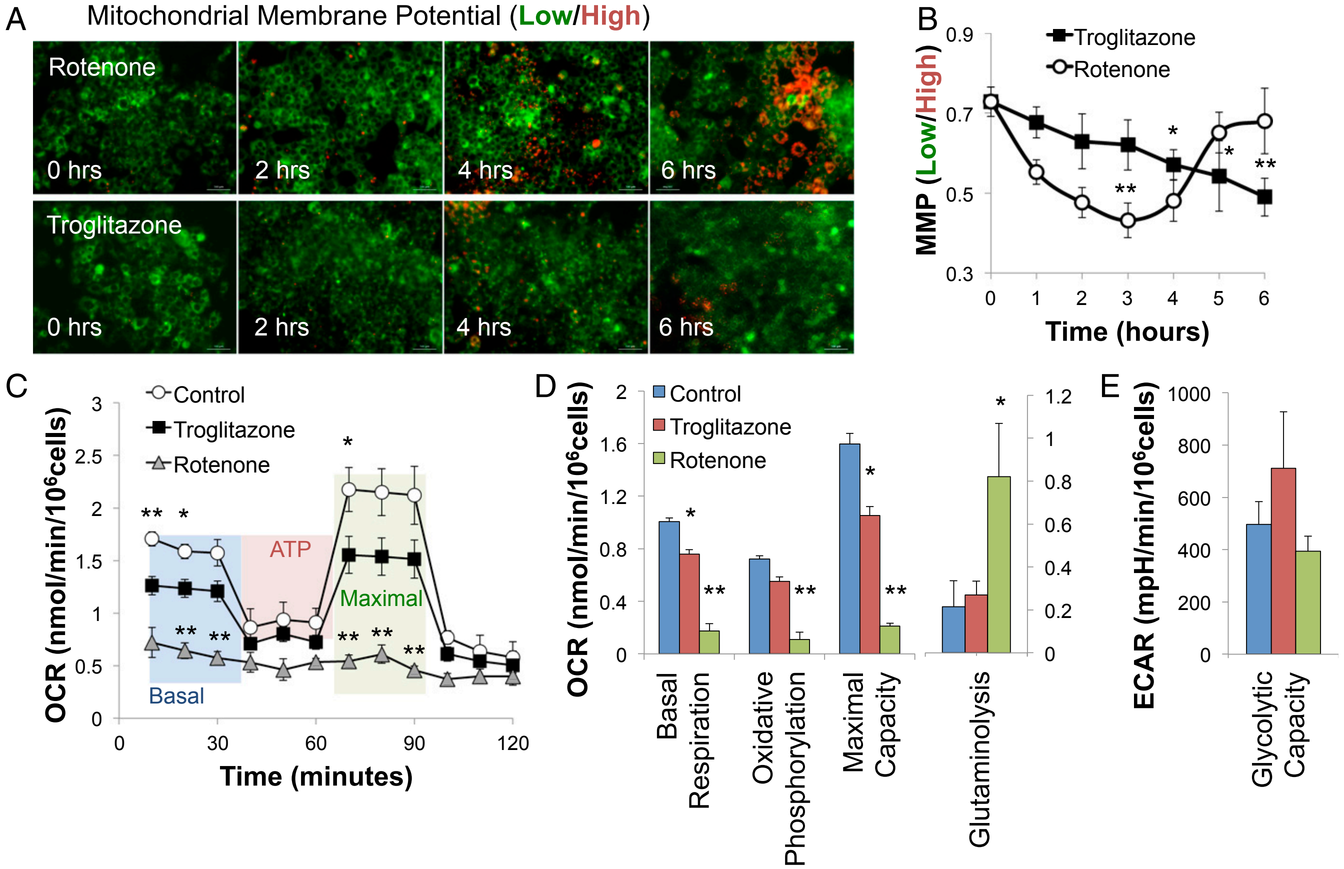

Fig. 6. (*A*) Live staining of HepG2/C3A cells with JC1 dye following exposure to 50 μM rotenone (*Upper*) or troglitazone (*Lower*). (*B*) Rotenone causes significant increase in MMP after 3 h of exposure ($P < 0.001$. $n = 3$). Troglitazone causes a gradual increase in MMP along 6 h of exposure ($P < 0.001$, $n = 3$). (*C*) Direct measurement of OCR using a Seahorse XF24 analyzer on HepG2/C3A cells exposed to 50 μM troglitazone, rotenone, or vehicle control. Basal respiration (blue) was measured for 30 min, showing significant differences between the three conditions ($P < 0.001$, $n = 3$). Oligomycin was injected at 30 min, blocking ATP production due to oxidative phosphorylation (red). FCCP was injected at 60 min, followed by complex I and III inhibitors at 90 min, showing differences in maximal mitochondrial capacity (green). (*D*) Troglitazone induced 20 ± 6% decrease in basal metabolic rate ($P < 0.01$, $n = 3$) and a 22 ± 9% decrease in maximal mitochondrial capacity ($P < 0.05$, $n = 3$) following FCCP injection. Rotenone induced 85 ± 5% decrease in oxidative phosphorylation ($P < 0.001$, $n = 3$) and 83%, 87% in basal and maximal capacity as well. Glutamine oxidation rate (glutaminolysis) is juxtaposed to the right showing nonsignificant 26 ± 30% increase following troglitazone treatment, but a 382 ± 115% increase due to rotenone exposure ($P < 0.03$, $n = 3$). (*E*) Extracellular acidification rate (ECAR), a surrogate measure of lactate production, increased by 43 ± 43% in troglitazone-treated cells, and decreased 21 ± 12% in rotenone-treated cells ($P > 0.17$, $n = 3$). *$P < 0.05$, **$P < 0.001$ by Student's *t* test.

potential (MMP) at regular intervals (Fig. 6*A*). Cells showed a rapid 40 ± 6% increase in MMP within 3 h of exposure to rotenone ($P < 0.001$, $n = 3$), but signal was rapidly lost due to cell death within 6 h. In contrast, exposure to troglitazone showed a steady 33 ± 7% increase in MMP over 6 h of exposure ($P < 0.001$, $n = 3$; Fig. 6*B*).

To demonstrate that altered MMP leads to the observed changes in metabolic pathways we used the Seahorse Flux Analyzer to measure changes in oxidative phosphorylation, glutaminolysis, and glycolysis on cells exposed to 50 μM of rotenone and troglitazone for 6 h (Fig. 6 *C*–*E*). As could be expected, rotenone induced 83 ± 5% decrease in mitochondrial basal metabolic rate ($P < 0.0002$, $n = 3$) and 85 ± 8% decrease in oxidative phosphorylation ($P < 0.0005$, $n = 3$). Glutaminolysis increased 4 ± 1 fold ($P < 0.03$, $n = 3$; Fig. 6*D*), whereas glycolytic capacity was relatively unchanged (Fig. 6*E*). Changes induced by troglitazone were milder, resulting in a 20 ± 6% decrease in mitochondrial basal metabolic rate ($P < 0.01$, $n = 3$), but no significant changes in glutaminolysis or glycolysis could be measured under static conditions, although both fluxes showed a mild up-regulation (Fig. 6 *D* and *E*).

Discussion

In this work we established a robust microfluidic platform combining liver-on-chip technology with automated microfluidic analysis of glucose metabolism and mitochondrial function (Fig. 1). Our system uses 1% DMSO to growth-arrest self-assembled aggregates of HepG2/C3A cells maintained under physiological conditions (Fig. 2). Cultures stabilized within 4 d displaying strong elevation of CYP450 expression (Fig. 2 *F* and *G*) and MRP2-active apical surfaces (Fig. 3*F*). At steady state, 13 ± 5% of the glucose consumed by growth-arrested HepG2/C3A cells in our bioreactor was directed toward oxidative phosphorylation with minor to negligible contributions from glutamine and lipid oxidation.

One advantage of our platform is the integration of medical-grade commercial sensors in a modular off-chip unit. These off-the-shelf components dramatically reduce fabrication costs and can be replaced as needed without pausing the experiment; this is particularly important with electrochemical sensors whose activity is dependent on membrane integrity and enzymatic function. Off-chip measurement also allowed us to automate sensor calibration, and create sharp chemical gradients, ensuring measurement stability for several days in culture, which stands in contrast to prior reports of integrated on-chip glucose and lactate sensors that offer

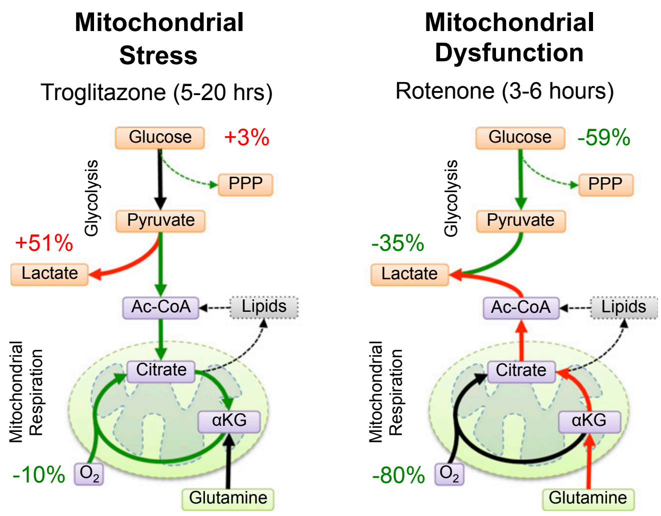

Fig. 7. Schematics depicting the metabolic response of liver cells to troglitazone-induced mitochondrial stress and rotenone-induced mitochondrial dysfunction compared with untreated controls. Down-regulated fluxes are shown in green, up-regulated fluxes are shown in red. Numbers reflect measured changes in glucose, lactate, and oxygen uptake.

less than 1–3 h of operation before signal drift requires recalibration (23). Stability of our sensors permitted over 24 h of continuous sampling (Fig. 5). In fact, though oxygen uptake dropped within minutes after exposure to rotenone and troglitazone (Fig. 3*H*), the metabolic shift from oxidative phosphorylation to glycolysis occurred only after 3 and 6 h of exposure, respectively (Fig. 5 *C*–*F*). Analysis of MMP showed a similar time frame and a gradual loss of function, coupled with a gradual change in glucose and lactate fluxes, suggesting that enzymatic rather than transcriptional changes are responsible for the metabolic shift. Change in glycolytic enzyme acetylation due to acetyl-CoA accumulation is one putative mechanism that requires further investigation.

A second advantage of our platform is the optical measurement of oxygen using tissue-embedded microsensors (Fig. 1). Optical sensors are advantageous over Clark-type electrodes because the latter consume oxygen during measurement and require frequent recalibration (12). Whereas standard optical sensors are affected by changes in optical focus, background, or particle migration, our approach focused on measurement of a phase-shift that is independent of changes in signal amplitude (11). Processes such as cell migration and necrosis that change the number and location of microbeads during the experiment have no effect on our measurement, permitting continuous measurements of oxygen uptake for over 28 d in vitro (Fig. 2*F*). In fact, our ability to measure oxygen uptake rates during stable stimulation stands in contrast to other approaches in the field that either circulate medium to increase signal intensity (24) or measure under static conditions (25) rather than at steady state.

The integration of both sensing modalities allowed us to identify differences in the metabolic response to rotenone and troglitazone that appear to be related to the severity of mitochondrial damage. Exposure to the antidiabetic drug troglitazone (Rezulin) induced the expected response as cells diverted glucose from metabolic pathways such as lipogenesis toward lactate, maintaining 97% of cellular ATP production and normal ATP/ADP ratio (Fig. 5*G*). This switch was not previously detected because the Warburg effect often dominates cell metabolism in culture and cell viability is unaffected. Though drug effect at this concentration appears minor, it could lead to an idiosyncratic response in compromised patients.

In contrast to the troglitazone response, cellular adaptation to rotenone-induced mitochondrial dysfunction was surprising. Cells showed a 59% decrease in glucose uptake, suggesting an accumulation of intermediates led to a block in downstream glycolysis. The switch to compensatory mechanisms was gradual, because lactate over glucose ratio increased above 2, and glutamine uptake increased, demonstrating a shift toward glutaminolysis (Fig. 6 *C*–*E*). Our results demonstrate the importance of monitoring all three fluxes because no combination of two measurements could reveal the entire picture.

In conclusion, our work demonstrates real-time measurement of glucose, lactate, and oxygen in a liver-on-chip bioreactor perfused under physiological conditions. Growth-arrested HepG2/C3A cells demonstrate long-term gene expression, polarization, and mitochondrial function for over 28 d in vitro. Automated electrochemical measurements are demonstrated for over 24 h in vitro. Our measurement allowed us to detect minute changes in the utilization of glucose occurring within 3 and 6 h after exposure to rotenone and troglitazone, respectively. The platform is uniquely able to monitor metabolic changes indicating mitochondrial dysfunction occurring at drug concentrations previously regarded as safe, as well as redistribution of ATP production under multiple conditions.

Materials and Methods

Bioreactor Fabrication. Bioreactors were fabricated from PMMA using computer numerical control (CNC) machining. Each unit was composed of two 50.8-mm circular support structures that fit standard 2-inch inserts, containing glass windows for microscopy. The bioreactor housed a removable polydimethylsiloxane (PDMS) microwell insert in which cells are protected from the negative effect of shear. Sealing around the microwells was realized with a rubber gasket creating an internal volume of 40 μL.

Removable Microwell Insert. PDMS microwell inserts were fabricated using laser cutting. Briefly, a thin sheet of PDMS (Dow Corning) was cast to 0.7 mm height using a motorized film applicator (Erichsen) and cured at 70 °C for 1 h. Microwells were cut to 1.5 mm diameter, and a center-to-center distance of 3 mm using a 355-nm pulsed Nd-YAG laser (3D-Micromac). PDMS inserts were washed with 70% (vol/vol) EtOH, nitrogen dried, and covalently bound to clean 0.5-mm thick glass coverslips (Schott) using oxygen plasma activation.

Cell Culture. HepG2/C3A cells were cultured under standard conditions in a humidified incubator at 37 °C, under 5% CO_2. Cells were obtained from the American Type Culture Collection. Cells were cultured in low-glucose modified Eagle medium supplemented with 10% (vol/vol) FCS, 100 U/mL penicillin, and 100 μg/mL streptomycin (Sigma-Aldrich). Medium was supplemented with 1% DMSO following bioreactor seeding to induce growth arrest and differentiation (16, 17).

Bioreactor Seeding. PDMS microwell inserts were sterilized with 70% EtOH and 30-min exposure to UV light before cell seeding. Cells were trypsinized, counted, and centrifuged at 300 × *g* for 5 min at 4 °C. The pellet was then mixed with 400 μg CPOx-50-RuP oxygen-sensing beads (Colibri Photonics) and resuspended in 100 μL of ice-cold solution of collagen type I (BD Biosciences) for a final seeding density of 4×10^6 cells/mL. The PDMS microwell insert was placed on ice and coated with ice-cold collagen solution for 5 min to remove air bubbles. Then 100 μL of collagen type I suspension containing cells and oxygen-sensing beads was layered on top the wells and incubated for 10 min on ice. The low temperature prevented premature collagen polymerization and the induction of cellular stress response pathways. Afterward, excess cell and microbead suspension was gently wiped off the microwell insert using a sterile glass coverslip leading to a concentration of 100,000 cells and 20 oxygen-sensing beads per well. Variance in cell density between individual wells and between bioreactors was less than 10% measured by DNA content. The inoculated microwell insert was then incubated for 5 min at 37 °C to polymerize the collagen. Following polymerization, the insert was immersed in 5 mL of cell culture medium and incubated for 20 min at 37 °C before being sealed in the bioreactor housing. Bioreactors were then placed in a climate control chamber (Evotec) on an IX81 fluorescence microscope (Olympus). Bioreactors were continuously perfused with cell culture medium noted above supplemented with 10 mM Hepes and 1% DMSO at a flow rate of 2 μL/min. The automated and motorized microscope stage was equipped with a holder for three microreactors, allowing three experiments to run simultaneously.

Quantitative RT-PCR. RNA was isolated and purified using Macherey–Nagel NucleoSpin RNA II kit according to manufacturer instructions. RNA concentration and purity was determined using NanoDrop ND-1000 spectrophotometer

(Thermo Fisher Scientific). cDNA was synthesized from 1 μg RNA sample using qScript cDNA SuperMix (Quanta BioSciences) according to the manufacturer's protocol. Gene expression analysis was carried out using KAPA SYBR FAST Universal 2× qPCR Master Mix (Kapa Biosystems) on BioRad CFX96 Real-Time System, according to manufacturer's directions. Gene transcription was evaluated using the ΔΔCt method normalized to 60S ribosomal protein L32 (RPL32) or ubiquitin C.

Finite Element Analysis. A computational fluid dynamic model was used to model pressure distribution, oxygen supply, and glucose consumption rates within the microwell bioreactor. A 3D model of the bioreactor geometry was designed and meshed using an extremely fine mesh of 5-μm tetrahedral elements. Finite element simulations were carried out using COMSOL Multiphysics 4.3b, coupling the Navier–Stokes equations with the convection and diffusion model for transport of oxygen and glucose. Inlet oxygen concentration was atmospheric 0.2 mM with a diffusion coefficient of 1.8×10^{-9} m^2/s. Oxygen uptake rate was measured to be 1.8×10^{-9} $mol \cdot min^{-1}$ per 10^6 cells. Inlet glucose concentration was 5.5 mM with a diffusion coefficient of 6×10^{-10} m^2/s, and uptake rate was measured under steady-state condition to be 2.4×10^{-9} $mol \cdot min^{-1}$ per 10^6 cells. Inlet lactate concentration was measured to be 1.5 mM, and production rate was measured to be 3×10^{-9} $mol \cdot min^{-1}$ per 10^6 cells under steady-state conditions.

Chemical Compounds. Troglitazone (T2573) and rotenone (R8875) were purchased from Sigma-Aldrich and diluted from H_2O or DMSO stock concentration 1:1,000 into HepG2/C3A culture medium. Exposure onset was calculated to within ±1 min based on volumetric flow rate, considering the length of the tubing and bioreactor volume.

Real-Time Oxygen Measurement. Real-time oxygen measurements were performed optically using lifetime-based luminescence-quenching as previously described (11). Briefly, 50-μm diameter polystyrene microbeads were loaded with ruthenium– phenanthroline-based phosphorescence dye (CPOx-50-RuP) that shows a decrease in phosphorescence decay time as a function of oxygen concentration (Fig. 1*C*). Excited by a sinusoidal amplitude-modulated 532-nm LED source, the microbeads emit a sinusoidal amplitude-modulated light at 605 nm that is shifted in phase due to oxygen quenching (Fig. 1*D*). To overcome the superposition of in-phase background fluorescence that alters the phase of the detected signal, we used a 53.5-kHz and 31.3-kHz two-frequency phase modulation, which allowed us to screen out background interference (26–28). Measurements were carried out by averaging five consecutive 3-s exposures, followed by 17-s intervals, for a total of 100 s. Measurements were taken every 15 min for as long as 28 d with no phototoxicity, signal drift, or relevant loss of signal intensity. The apparatus consists of the OPAL package (Colibri Photonics) that is comprised of a control module, 532-nm LED, and a photomultiplier detector mounted on the ocular of an IX83 Olympus microscope (Olympus). A filter cube with 531/40 (excitation), 607/70 (emission) was inserted in the optical light path during measurements.

Evaluation of Toxicological End Points. PMDS microwell inserts were removed from the bioreactor following 24-h exposure to rotenone or troglitazone. Cholestasis was evaluated using 5(6)-carboxy-2′,7′-dichlorofluorescein diacetate (CDFDA) cell-permeable dye that is metabolized to fluorescent CDF and secreted to active bile canaliculi by active multidrug resistance-associated protein 2 (MRP2). Briefly, cells were incubated with 2 μg/mL of CDFDA and 1 μg/mL of Hoechst 33342 for 20 min, and washed with PBS. Number of bile canaliculi foci was normalized for number of Hoechst-labeled nuclei. Apoptosis was evaluated using DeadEnd fluorometric TUNEL system (Promega) according to manufacturer directions. Briefly, cells were fixed in 4% (wt/vol) paraformaldehyde, permeabilized, and exposed to fluorescein-12-dUTP and terminal deoxynucleotidyl transferase, dyeing apoptotic nuclei green. The reaction was subsequently stopped and the cells counterstained for Hoechst. A percent apoptotic nucleus was calculated by dividing the number of TUNEL to Hoechst-positive nuclei.

Measurement of Mitochondrial Stress in Isolated Mitochondria. Mitochondria were isolated using a Mitochondria Isolation Kit (Abcam) per manufacturer instructions. Briefly, 10^7 cells were collected and ruptured using 30 strokes in a precooled dounce homogenizer. Homogenate was centrifuged twice at 1,000 × *g* for 10 min at 4 °C to remove debris, and finally at 12,000 × *g* for 15 min at 4 °C. Pellet containing the isolated mitochondria was resuspended in a protease inhibitor mixture. Protein concentration was determined using Bradford. A total of 20 μg of mitochondrial protein per well was plated in gelatin-coated SeaHorse XFp cell culture miniplate and centrifuged at 3,000 × *g* for 20 min at 4 °C in mitochondrial assay solution as previously described (29). Oxygen consumption rate (OCR) was measured by the XFp Extracellular Flux Analyzer (Seahorse Biosciences). Mitochondrial activity was profiled by successive injections of ADP (Sigma-Aldrich) and 50 μM of troglitazone, rotenone, or DMSO control.

Microfluidic Switchboard Fabrication. A computer-controlled microfluidic switchboard carried out automated sampling, calibration, and washing of the amperometric sensor unit, fabricated using two-layer soft lithography. Briefly, an adherent layer of hexamethyldisilazane (Sigma-Aldrich) was spin coated at 4,000 rpm for 30 s. Four layers of AZ-4652 (MicroChem) were sequentially spin coated at 800 rpm for 40 s, baked for 5 min at 100 °C, and exposed to UV light for 90 s. Curved AZ-4652 flow channels were molded by reflow using a gradual temperature increase of 35 °C to 150 °C over 3 h followed by hard-baked overnight at 150 °C. AZ-4652 channels dimensions were measured to be 100 × 25 μm (width × height). Control layer was fabricated separately using SU-8 photoresist (MicroChem), spin coated to 100-μm height, prebaked for 25 min at 100 °C, exposed to UV light for 15 s, and postbaked for 12 min. Top layer SU-8 control channels dimensions were 100 × 100 μm (width × height). Master molds were treated with trichlorosilane (Sigma-Aldrich) for easier removal of PDMS after curing. Each layer was cast separately by replica molding, aligned, and bonded via curing agent diffusion as previously described (30). The microfluidic switchboard was finally bonded to glass using oxygen plasma activation. The final device consists of 11 inlets and a common outlet that are regulated by self-addressable micromechanical valves.

Flow System and Microcontroller. Dedicated microfluidic controller and flow circuit was previously described in detail (13). Briefly, digitally controlled solenoid valves (Festo) were assembled into two pressure manifolds with a linear range of 0.15–6 bars. One manifold was connected to fluid reservoirs (Fluigent) perfusing the bioreactor, washing solution, atmospheric air, and calibration buffers. The second manifold was used to actuate the switchboard's control channels with a pressure of 1.05 bar. The switchboard flow outlet was connected to the PMMA housing of the amperometric sensors unit.

Real-Time Glucose and Lactate Measurements. Amperometric glucose and lactate sensors were purchased from BioSensor Technology and embedded in a CNC-fabricated PMMA flow-chamber with an inner volume of 26 μL. The sensors are based on the enzymatic reactions of glucose oxidase, with a linear range of 0.5 mM to 30 mM, and lactate oxidase, with a linear range of 0.5 mM to 20 mM. Both sensors produce H_2O_2 in amounts proportional to the measured metabolite, which is detected with platinum electrodes under polarized condition. The microfluidic controller (13) was programmed to open a microfluidic valve every hour, allowing a 40-μL medium sample to flow through the switchboard and into the sensors unit. Amperometric measurement lasted 200 s and was followed by automated perfusion of PBS washing solution, CAL 4+M calibration buffer (Eschweiler), and 4 s of air bubble acting as a diffusion barrier between samples. Reading was carried out on EmStat3 OEM embedded potentiostat (PalmSens) connected to the central computer.

Assessment of Cell Viability. Unless otherwise noted, cell viability was determined using a LIVE/DEAD Cytotoxicity kit (Molecular Probes) according to manufacturer's instructions. In brief, cultures were incubated with 2 μM Calcein AM and 3 μM ethidium homodimer-1 for 25 min. Hydrolysis by functional intracellular esterases causes live cells to fluoresce green, while the punctured membranes of dead cells permit ethidium homodimer-1 to bind DNA and fluoresce red. Cellular viability was calculated by live to dead ratio and normalized to negative control.

Quantification of ATP/ADP Ratio. Intracellular ATP and ADP quantification was carried out using Abcam ADP/ATP Assay Kit (ab65313) according to manufacturer's instructions. Briefly, reaction buffer was preincubated at room temperature for 2 h before beginning of measurements, to burn off low-level ATP contamination, as suggested by the manufacturer. Cells were incubated in nucleotide releasing buffer for 5 min at room temperature, with gentle shaking. Background bioluminescence reading of the reaction mix was taken for calibration, followed by 2 min incubation of 50 μL sample solution in each reaction well, and a bioluminescence reading to measure cellular ATP content. ADP converting enzyme was then added, as instructed, following incubation of 2 min at room temperature to measure total ADP + ATP.

Measurement of Oxidative Phosphorylation and Mitochondrial Stress. HepG2/C3A cells were plated in gelatin-coated SeaHorse XFp cell culture miniplates (Seahorse Bioscience) and cultured for 24 h. Subsequently, cultures were treated with medium containing 50 μM troglitazone for 6 h, 50 μM rotenone for 3 h, or vehicle control before initiation of assay. Mitochondrial stress test assay was conducted per manufacturer instructions (29). Briefly, cells were incubated in unbuffered XF Base Medium supplemented with 2 mM glutamine, 1 mM sodium pyruvate, and 10 mM glucose (pH 7.4) for 1 h at 37 °C in a non-CO_2 incubator. Basal OCR was measured for 30 min, followed by injection of 1 μM oligomycin, a mitochondrial complex IV inhibitor that completely blocks oxidative phosphorylation. The decrease in OCR due to oligomycin treatment is defined as oxidative phosphorylation rate. A total of 1 μM carbonyl cyanide-4 (trifluoromethoxy) phenylhydrazone (FCCP), an uncoupling agent, is added at 60 min to measure maximal mitochondrial activity followed by complete inhibition at 90 min using a mixture of 0.5 μM antimycin A and rotenone, mitochondrial complex III and complex I inhibitors. Basal extracellular acidification rates (ECAR) was measured for 30 min, in the presence of 10 mM glucose, followed by injection of 1 μM oligomycin. The increase in ECAR due to oligomycin treatment was defined as glycolytic capacity. Data are presented normalized to 10^6 cells as determined by Hoechst DNA content assay.

Measurement of Glutamine Oxidation. HepG2/C3A cells were plated in gelatin-coated XFp cell culture miniplates and cultured for 24 h. Subsequently, cultures were treated with medium containing 50 μM troglitazone for 6 h, 50 μM rotenone for 3 h, or vehicle control before initiation of assay. Glutamine oxidation assay was conducted per manufacturer instructions. Briefly, cells were incubated in unbuffered XF Base Medium supplemented with 2 mM glutamine, 1 mM sodium pyruvate, and 10 mM glucose (pH 7.4) for 1 h at 37 °C in a non-CO_2 incubator. Glutamine oxidation was profiled by successive injections of 3 μM BPTES, an allosteric inhibitor of glutaminase (GLS1), and a mixture of 4 μM etomoxir, a carnitine palmitoyl-transferase 1A (CPT1A) inhibitor and 2 μM UK5099, a mitochondrial pyruvate carrier inhibitor, blocking fatty acid oxidation and oxidative phosphorylation, respectively. The decrease in baseline OCR due to BPTES treatment was defined as the rate of glutaminolysis. Data are presented normalized to 10^6 cells as determined by Hoechst DNA content assay.

Evaluating Mitochondrial Membrane Potential. JC-1 cell-permeable dye was purchased from Life Technologies. HepG2/C3A cells were incubated with 50 μM of troglitazone or rotenone for varying durations. To evaluate mitochondrial membrane potential at each time point, cells were incubated with 5 μM JC-1 dye for 30 min, washed with PBS, and imaged by confocal microscopy on a LSM700 (Zeiss). The JC-1 dye exhibits potential-dependent accumulation in mitochondria, indicated by a fluorescence emission shift from 529 to 590 nm due to the formation of J-aggregates. Consequently, mitochondrial depolarization is quantified by dividing red over green fluorescence intensity.

Metabolic Pathways and ATP Production. Glucose uptake, oxygen uptake, and lactate production rates were measured by calculating the change in metabolite concentration between the bioreactor in- and outflow as function of perfusion rate and cell number as described above. Metabolic rates were calculated assuming negligible contribution to oxygen uptake by fatty acid oxidation and enzymatic activity. Low level of lipids in our culture medium ensured that fatty acid uptake was 50-fold lower than glucose, whereas glutamine contribution to the Krebs cycle was minor (*Results*). Periodic acid–Schiff (PAS) staining showed no significant change in glycogen content following 12-h exposure to the drugs (Fig. S1).

Based on these assumptions, oxidative phosphorylation flux was calculated by dividing the oxygen uptake rate by six. We estimated 32 ATP molecules generated by complete oxidation of one molecule of glucose. Glycolysis flux was calculated by dividing lactate production rate by two, with maximal rate defined by glucose uptake rate minus the oxidative phosphorylation flux. ATP production in glycolysis was estimated to be two molecules per molecule of glucose. We assumed that any glucose left over was directed toward lipogenesis, because the contribution of pentose phosphate pathway in nonproliferating cells is minor (31). Finally, we assumed that excess lactate was produced by glutaminolysis, and confirmed our assumption using offline measurement of glutamine uptake (Fig. S2). ATP production in glutaminolysis was estimated to be three molecules per molecule of lactate generated.

Statistical Analysis. Experiments were repeated 2–3 times with triplicate samples for each experimental condition. Data from representative experiments are presented, whereas similar trends were seen in multiple trials. A parametric two-tailed Student's *t* test was used for calculating significant differences between groups. All *n* values represent the number of biological samples analyzed per condition. All error bars indicate ± SD.

ACKNOWLEDGMENTS. The authors thank Ms. Rotem Karp and Dr. Elmar Schmaelzlin (Colibri Photonics GmbH) for technical support and the generous gift of Sam and Rina Frankel. This work was funded by ERC Starting Grant TMIHCV 242699, the British Council BIRAX Regenerative Medicine Award 33BX12HGYN, and the HeMibio consortium, funded by the European Commission and Cosmetics Europe as part of the SEURAT-1 Cluster Grant HEALTH-F5-2010-266777.

1. Huh D, et al. (2010) Reconstituting organ-level lung functions on a chip. *Science* 328(5986):1662–1668.
2. Monga SP, et al. (2005) Mouse fetal liver cells in artificial capillary beds in three-dimensional four-compartment bioreactors. *Am J Pathol* 167(5):1279–1292.
3. Allen JW, Bhatia SN (2003) Formation of steady-state oxygen gradients in vitro: Application to liver zonation. *Biotechnol Bioeng* 82(3):253–262.
4. Khademhosseini A, et al. (2005) Cell docking inside microwells within reversibly sealed microfluidic channels for fabricating multiphenotype cell arrays. *Lab Chip* 5(12):1380–1386.
5. Sivaraman A, et al. (2005) A microscale in vitro physiological model of the liver: Predictive screens for drug metabolism and enzyme induction. *Curr Drug Metab* 6(6): 569–591.
6. Adeleye Y, et al. (2015) Implementing toxicity testing in the 21st century (TT21C): Making safety decisions using toxicity pathways, and progress in a prototype risk assessment. *Toxicology* 332:102–111.
7. Vinken M (2013) The adverse outcome pathway concept: A pragmatic tool in toxicology. *Toxicology* 312:158–165.
8. Nelms MD, et al. (2015) Proposal of an in silico profiler for categorisation of repeat dose toxicity data of hair dyes. *Arch Toxicol* 89(5):733–741.
9. Moussaieff A, et al. (2015) Glycolysis-mediated changes in acetyl-CoA and histone acetylation control the early differentiation of embryonic stem cells. *Cell Metab* 21(3): 392–402.
10. Vinken M (2015) Adverse outcome pathways and drug-induced liver injury testing. *Chem Res Toxicol* 28(7):1391–1397.
11. Prill S, et al. (2015) Real-time monitoring of oxygen uptake in hepatic bioreactor shows CYP450-independent mitochondrial toxicity of acetaminophen and amiodarone. *Arch Toxicol*, 10.1007/s00204-015-1537-2.
12. Alborzinia H, et al. (2011) Real-time monitoring of cisplatin-induced cell death. *PLoS One* 6(5):e19714.
13. Ezra E, et al. (2015) Microprocessor-based integration of microfluidic control for the implementation of automated sensor monitoring and multithreaded optimization algorithms. *Biomed Microdevices* 17(4):82.
14. Rowlands JC, Sander M, Bus JS; FutureTox Organizing Committee (2014) FutureTox: Building the road for 21st century toxicology and risk assessment practices. *Toxicol Sci* 137(2):269–277.
15. Tilles AW, Baskaran H, Roy P, Yarmush ML, Toner M (2001) Effects of oxygenation and flow on the viability and function of rat hepatocytes cocultured in a microchannel flat-plate bioreactor. *Biotechnol Bioeng* 73(5):379–389.
16. Sainz B, Jr, Chisari FV (2006) Production of infectious hepatitis C virus by well-differentiated, growth-arrested human hepatoma-derived cells. *J Virol* 80(20): 10253–10257.
17. Fiore M, Zanier R, Degrassi F (2002) Reversible G(1) arrest by dimethyl sulfoxide as a new method to synchronize Chinese hamster cells. *Mutagenesis* 17(5):419–424.
18. Cukierman E, Pankov R, Stevens DR, Yamada KM (2001) Taking cell-matrix adhesions to the third dimension. *Science* 294(5547):1708–1712.
19. Baharvand H, Hashemi SM, Kazemi Ashtiani S, Farrokhi A (2006) Differentiation of human embryonic stem cells into hepatocytes in 2D and 3D culture systems in vitro. *Int J Dev Biol* 50(7):645–652.
20. Siddiqui MA, et al. (2013) Rotenone-induced oxidative stress and apoptosis in human liver HepG2 cells. *Mol Cell Biochem* 384(1-2):59–69.
21. Julie NL, Julie IM, Kende AI, Wilson GL (2008) Mitochondrial dysfunction and delayed hepatotoxicity: Another lesson from troglitazone. *Diabetologia* 51(11):2108–2116.
22. Masubuchi Y (2006) Metabolic and non-metabolic factors determining troglitazone hepatotoxicity: A review. *Drug Metab Pharmacokinet* 21(5):347–356.
23. Eklund SE, et al. (2009) Metabolic discrimination of select list agents by monitoring cellular responses in a multianalyte microphysiometer. *Sensors (Basel)* 9(3):2117–2133.
24. Domansky K, et al. (2010) Perfused multiwell plate for 3D liver tissue engineering. *Lab Chip* 10(1):51–58.
25. Beeson CC, Beeson GC, Schnellmann RG (2010) A high-throughput respirometric assay for mitochondrial biogenesis and toxicity. *Anal Biochem* 404(1):75–81.
26. Ast C, Schmälzlin E, Löhmannsröben HG, van Dongen JT (2012) Optical oxygen micro- and nanosensors for plant applications. *Sensors (Basel)* 12(6):7015–7032.
27. Schmälzlin E, et al. (2005) An optical multifrequency phase-modulation method using microbeads for measuring intracellular oxygen concentrations in plants. *Biophys J* 89(2):1339–1345.
28. Lohmannsroben HG, Beck M, Hildebrandt N, Schmalzlin E, van Dongen JT (2006) New challenges in biophotonics: Laser-based fluoroimmuno analysis and in-vivo optical oxygen monitoring. *SPIE Proc*, 10.1117/12.663583.
29. Zhang J, et al. (2012) Measuring energy metabolism in cultured cells, including human pluripotent stem cells and differentiated cells. *Nat Protoc* 7(6):1068–1085.
30. Melin J, Quake SR (2007) Microfluidic large-scale integration: The evolution of design rules for biological automation. *Annu Rev Biophys Biomol Struct* 36:213–231.
31. Ouattara DA, et al. (2012) Metabolomics-on-a-chip and metabolic flux analysis for label-free modeling of the internal metabolism of HepG2/C3A cells. *Mol Biosyst* 8(7): 1908–1920.